Bubble Evolution and Anode Surface Properties in Aluminium Electrolysis

Rebecca Jayne Thorne[1*], Camilla Sommerseth[1], Arne Petter Ratvik[2], Stein Rørvik[2], Espen Sandnes[3], Lorentz Petter Lossius[3], Hogne Linga[3] and Ann Mari Svensson[1]

[1]Dept. of Materials Science and Engineering, Norwegian University of Science and Technology, NO-7491 Trondheim, Norway

[2]SINTEF Materials and Chemistry, NO-7465 Trondheim, Norway

[3]Norsk Hydro ASA, NO-6881 Årdalstangen, Norway

[*]Corresponding author. Tel: +47 400 85886. Email: rjt@nilu.no. Present address: Department of Environmental Impacts and Economics (IMPEC), Norwegian Institute for Air Research (NILU), PO Box 100, NO-2027 Kjeller, Norway

Keywords: Carbon anode, aluminium electrolysis, bubble, wettability, isotropy, roughness, porosity

Abstract

One significant contribution to the anodic potential during aluminium electrolysis is the formation of CO_2 bubbles that screen the anode surface. This effect creates an additional ohmic resistance as well as an increased reaction overpotential, hyperpolarisation, as the effective surface area decreases. This work aims to improve the understanding of how anode properties - including isotropy at the optical domain level, wettability (towards electrolyte), surface roughness and porosity - affect bubble

evolution. Pilot anodes, made with single source coke types varying in isotropy, were used to study bubble evolution by electrochemical methods. In order to retain bubbles during experiments, anodes were designed to have only horizontal surface area. Bubble formation and release were monitored at different current densities, and were tracked by measuring the oscillations in anode potential and series resistance. Anodes made from different cokes were found to have different bubble evolution properties, possibly due to variation in the density of nucleation sites at the surface of each anode and varying anode-electrolyte wettability.

1. Introduction

Reducing energy consumption in industrial aluminium electrolysis is a major concern and challenge, both for cost and environmental considerations [1, 2]. A large part of the cell voltage of a relatively modern industrial aluminium cell (approximately 4.3 V) is associated with the carbon anode, of which 0.3-0.6 V is the anode overpotential.

During aluminium electrolysis oxide ions from the dissolution of alumina in cryolite are discharged electrolytically and form CO_2 on the carbon anode, made from coke and a pitch binder, whilst aluminium metal is formed on the cathode. Some studies show that CO is also formed at the anode, especially at low current densities [3, 4], and other gases including the perfluorocarbon gases CF_4 and C_2F_6 are formed at higher anode potentials during anode effect [5-9]. Gas bubbles are thought to nucleate at specific sites on the anode surface by (non-classical) heterogeneous nucleation [10, 11], and grow spherically or semi-spherically, before detaching and moving to coalesce with other bubbles. Bubbles then roll along the anode surface and

are released at the anode edge [3, 12]. On small anodes this process is sequential, but with intermediate size or industrial anodes, typical behaviour is less periodic and multiple bubbles are released [13]. Previously, bubbles have been monitored through direct visual/X-ray observation [14-16], bath height fluctuation [3], current interruption and/or associated resistance [3, 4, 17, 18] and potential oscillation [19-22]. Most studies suggest that bubble layer thickness is around 5 mm in both laboratory [3, 12, 16, 23] and industrial [3, 14, 16, 24] cells, although there is some variation reported [25, 26].

Gas produced at the anode causes an additional voltage loss. Two dominating effects are observed; an increase in ohmic resistance, mainly caused by the reduced effective anode surface area, and an increase in the overpotential due to higher current density at the remaining surface. The first part is observed as an increase in the series resistance, i.e. $R_s = R'_s + \delta R_s$, where R'_s equals the series resistance with no bubbles screening the surface. The second part is observed as an increase in the reaction overpotential, a specific charge transfer overpotential term relating to electrode reactions where intermediate adsorption/desorption plays a decisive role. The additional overpotential due to the reduced effective surface area caused by bubble screening of the anode is commonly denoted hyperpolarisation, η_h [27, 28]. In a similar representation as above, $\eta_r = \eta'_r + \eta_h$, where η'_r equals the reaction overpotential with no bubble screening of the anode surface. The concentration overpotential at the anode, η_c, in this system may be considered as negligible [29]. When measuring the uncompensated anode potential versus a reference electrode, the potential can be expressed as Equation 1 below. E^{rev} is the reversible potential for the CO_2 forming reaction and I is the current.

$$E_{anode,\ measured} = E^{rev} + \eta_c + \eta'_r + \eta_h + I\cdot(R'_s + \delta R_s) \qquad (1)$$

The additional voltage loss due to bubbles has been shown to be highly dependent on anode geometry and orientation. Measurements by Leistra and Sides using rotating vertical anodes with a diameter of 1.27 cm^2 showed that the hyperpolarisation caused by bubbles at 1 A cm^{-2} is only around 8 mV [27, 29] or 20 mV [28]. The authors related these potential differences to a 20 % reduction in effective surface area [27, 28]. Using a graphite rod with 18 mm diameter, Cassayre et al. [16, 23] found that bubbles as small as 2-3 mm were released from vertical surfaces, but bubbles were ~12 mm before being released from underneath (at 1 A cm^{-2}). On large industrial anodes with a high proportion of horizontal surfaces, an extra ohmic voltage drop due to bubbles has been estimated in the range of 0.15-0.35 V [26]. To improve anode geometry for more favourable bubble release and to reduce the effect of bubbles on potential, slots are cut in industrial anodes [23, 30-32]. In one study by Wang et al. [33], a particular type of slot was shown to reduce the bubble-related voltage drop from ~0.24 V to 0.08 V.

In addition to anode geometry, it is thought that surface topography and other properties of the anode can have dramatic effects on the nature of bubbles released. Bubbles nucleate at specific sites on an anode, dependent on its microstructure, and typically on defect sites or in pores [4, 10, 34]. Generally one bubble is assumed to nucleate per pore. Subsequent to nucleation, local bubble motion is thought to be controlled by many factors including anode shape, roughness, surface tension, bath (and metal) flow and the contact angle between anode and electrolyte [35]. In a study

by Peterson et al. [22], small bubbles that detached rapidly from the anode were produced when the anode-electrolyte contact angle was small, achieved by using an inert anode material. With the same reasoning, it was suggested by Cassayre et al. [16] that bubbles growing on carbon anodes with poor electrolyte wetting were stuck and required growth before detachment. Anode-electrolyte wetting is also the main reason suggested by Gao et al. [14] for the differences in bubble behaviour seen with either carbon, metal or ceramic-metal anodes in their see-through cell study; similar to Peterson et al. [22], they found that the bubble induced voltage was lower on inert anodes than carbon, suggesting that bubbles are smaller. When investigating the effect of granulometry on bubble evolution, Kasherman and Skyllas-Kazacos [17] found that an industrial anode with a large coke fine fraction and porous appearance produced bubbles that gave lower resistivity, and thus less screening of the anode, than an anode with optimum granulometry and pitch content, or graphite. The authors suggested that this was because the latter anodes produced bubbles with a higher dynamic gaseous volume fraction, possibly due to smaller bubbles that travelled more slowly, and/or differences in anode-electrolyte wetting. Aside from microstructure and wetting, other specific effects relating to changes of coke type remain unknown - understanding this relationship is particularly important due to variation in the quality of cokes available for anode production [36-38].

This work aimed at describing how differences in the coke type used for fabrication of the anode affect bubble formation and release, and thus the magnitude of the bubble-related voltage loss. The cokes used were single source cokes varying in isotropy, where isotropy is defined in terms of the optical domains which form during the semi-liquid mesophase stage preceding carbonisation, where the size of domains is

determined by how far the melting together, or coalescence, of mesophase droplets progresses. A series of anodes varying only in the coke type was produced, and anodes were characterised with respect to porosity, surface roughness, pore size distribution and electrolyte wetting properties. Bubble evolution was studied by electrochemical techniques using horizontal anode geometry. Bubbles were monitored via their associated oscillation in potential or series resistance, providing information about the relative screening of the surface by bubbles and size of the bubbles released, which were again compared to the anode physical properties. Although the study cannot be directly compared to industrial situations (as it focuses on the initial period of electrolysis when the anode surface was retained close to the original shape, and the coke aggregate size was artificially limited at 0-2 mm), these fundamental relationships are nevertheless important to explore.

2. Materials and Methods

The anodes used in this study comprised of pilot scale anodes produced by Norsk Hydro ASA from five single source cokes that varied in isotropy (particle size 2-0 mm), as described previously [39, 40]. Anodes 1-4 were made from petroleum cokes and Anode 5 from a coal tar pitch based coke. Aside from coke type, all other production parameters were constant. In addition, a graphite material was included for study (Ultrapure grade CMG provided by Svensk Specialgrafit AB).

2.1. Characterisation of anode surface and interfacial properties

Anodes were routinely characterised for density and permeability according to ISO 12985-1 and a Norsk Hydro ASA in house method similar to ISO 15906 respectively.

Anode impurities (metal and sulphur content) were additionally characterised using an X-ray fluorescence method according to ISO 12980.

Other properties not routinely measured in industry are also important for the understanding of electrochemical behaviour and bubble evolution. These include anode porosity, isotropy, real surface area and wetting properties of the anode-electrolyte-gas interface. Isotropy was determined using optical microscopy (high-end Leica/Relchert MeF3A metallurgical optical reflecting light microscope), by producing compound images from 192 individual frames. These were taken by mounting fluorescent epoxy-embedded and polished (to 1 µm) cylindrical samples in a holder and scanning across the total surface at magnifications of x100 and x250 under ultraviolet or polarised light, respectively. Analysis software, developed by Rørvik et al. [41, 42], was subsequently used on the individual images to describe the pore distribution and the texture. The pore size distribution was reported as the sum of the pore area in 2D for each respective pore size; an approximation proportional to volume in 3D. Two different mounted and polished samples were analysed for each anode material.

The surface roughness of un-mounted anode sections was studied using confocal microscopy (Infinitefocus Alicona, optical 3D surface metrology), to obtain the ratio of real (3D): geometric (2D) surface area at a resolution of 410 nm. These samples were the counterpart-cuts of those used later for electrochemical measurements, and are thus representative of the fresh anode surface during electrolysis in this study. Two samples with 8 mm diameter (0.50 cm^2) were measured for each anode material.

The wetting of anodes with electrolyte was studied using sessile drop contact angle measurements. Alumina-saturated cryolite from electrochemical experiments (see section 2.2 for details) was sectioned into pieces weighing ~0.03 g. The cryolite pieces were put on the surface of polished cylindrical sections of anodes (diameter 10 mm, thickness 5 mm, 800 grit SiC paper), and situated in a tube furnace with camera (firewire digital video camera with telecentric lens). The contact angle of the electrolyte on the carbon was studied whilst heating between 900 °C and 1000 °C at 5 °C min^{-1} in an argon atmosphere. Two replicates were performed using different samples for graphite, and one for the pilot anodes.

2.2. Electrochemical measurements of bubble evolution

Anode materials were cut and assembled as illustrated in Figure 1a and b. Sides were shielded using silicon nitride in order to expose only the 8 mm diameter (0.50 cm^2 area) horizontal base when immersed in the melt. Due to this horizontal design, bubble retention on the base of the anode was maximised for bubble study, i.e. large potential oscillations were observed during electrolysis. This was verified by comparing the horizontal graphite anode against graphite anodes with vertical sides and a graphite rod, as described in [40] and [39] respectively. Additionally, horizontal graphite anodes with diameter 6, 10 or 14 mm were tested in order to verify that the selected geometry did not affect the results.

To ensure that the permeability of the anodes did not affect the dominant way that CO_2 was released from the anode, Equation 2 [43] was used to calculate the volume of gas that could potentially escape through anode pores. Here, μ is material permeability (m^2), V is the volume of gas flowing through the material (m^3), t is the

time in which gas flows through material (s), η is dynamic viscosity of CO_2 (Pa s), δ is the material thickness that gas flows through (m), A is the cross-sectional surface of the material that gas flows through (m^2), P is the absolute pressure of the gas (Pa) and P_1-P_2 is the overpressure (Pa). To estimate the overpressure, the hydrostatic pressure was calculated according to Equation 3, where P is the hydrostatic pressure (Pa), h is the column height (m), ρ is the density (kg m^{-3}) and g is the gravitational constant (m s^{-2}).

$$\mu = \frac{V}{t} \cdot \eta \frac{\delta}{A} \cdot \frac{1}{P_1 - P_2} \cdot \frac{2P}{P_1 - P_2} \quad (2)$$

$$P = h \cdot \rho \cdot g \quad (3)$$

Electrochemistry was performed in a cryolite melt with a molar ratio of sodium fluoride to aluminium fluoride (cryolite ratio, CR) of 2.3 (Sigma Aldrich >97 %) corresponding to 9.8 wt% excess AlF_3 (industrial grade, sublimed in-house), and 9.4 wt% ɣ alumina (Merck). A schematic of the experimental cell is shown in Figure 1c, which was contained within a tube furnace at 1000 °C in an argon atmosphere. Electrochemical characterisation was performed using a Zahner IM6 with built in Electrochemical Impedance Spectroscopy (EIS) module and 20 A booster (PP201, Zahner-Elektrik).

Anode potential was measured with respect to an aluminium reference electrode (described in [6]), whilst applying a current between the anode and graphite crucible. All potentials in this study are therefore quoted w.r.t Al. Various current densities were applied, ranging from 1 A cm^{-2} to 0.1 A cm^{-2}. Potential oscillations arising from bubble formation and release were studied once the process had reached a pseudo-

steady state after 200 seconds. The volume of bubbles released over time was calculated from the time interval for one complete potential oscillation, relating to the charge passed and assuming a pressure of 1 atm. At the same current densities, EIS was used to measure spectra between 100,000 Hz and 0.1 Hz, as well as tracking R_s over time. For the latter measurements, impedance was measured at a constant high frequency directly corresponding to R_s; frequency values were determined from the high frequency X-axis intercept on Nyquist spectra. Due to constraints of sampling intervals, R_s could only be tracked when bubbles were released at a low frequency, i.e. at low current densities. Additionally, cyclic voltammetry (CV) was performed at 0.1 V s^{-1} between the open circuit potential (OCP) and 2.5 V, as previous experiments showed that sweep-rates up to 0.1 V s^{-1} gave similar results compared to steady-state polarisation curves. Three or more sample parallels were performed for each anode within these randomised series, and the order of the anode materials tested was randomised to eliminate possible changes in the characteristics of the melt over time.

3. Results and discussion

3.1. Characterisation of anode surface and interfacial properties

Characteristic properties of the anodes are given in Table 1. Anodes 3-5 had low fibre index and high mosaic index, parameters described in [42] relating to the alignment and fineness of the optical domains respectively, and were therefore the most isotropic. As expected, these anodes also had the highest levels of impurities. Metal and sulphur impurities generally correlated, although Anode 5 - made from a pitch based coke - was high in metal impurities but low in sulphur. Densities were similar,

but anodes made from the most isotropic cokes (Anodes 3-5) had the highest permeability.

The total porosity (Figure 2) calculated using image analysis software, was relatively similar for the industrial coke-based anodes, with only small variation reflecting the densities shown in Table 1. However, the relative pore size distribution for each anode varied (Figure 3a). Figure 3b shows the approximate number of pores of each size for an anode with 8 mm diameter; the size used for electrochemical testing, as determined from data in Figure 3a. Anodes made from more isotropic cokes had a higher content of larger pores (modal diameter on a logarithmical scale ~80 μm), whereas less isotropic coke anodes had a higher content of smaller pores (modal diameter on a logarithmical scale ~10 μm). Unlike the other anodes, graphite had a very high proportion of small pores (<10 μm), which led to issues of poor epoxy penetration and possible analysis inaccuracy.

There was also a variation in the specific location of the pores amongst the anodes (Figure 4). Anodes made from more isotropic cokes tended to have a more inhomogeneous distribution of pores, which were located only around the edges of particles. This was in contrast to the more anisotropic anodes which had pores fairly well distributed over the whole surface, including within the coke grains. These differences may be due to variation in packing density of the coke fines used to make the anode, possibly related to differences in particle shape, and differences in the densities of the coke particles themselves. The lower the internal porosity of the cokes, the greater the porosity difference between the coke and the binder phase. Additionally, for the more isotropic cokes, the adherence between the binder phase

and the coke grains was poor compared to the more anisotropic grains, probably related to the smoother surface of the isotropic cokes.

The real to geometric area ratio of the anodes is shown in Figure 5. For each anode, the entire 0.50 cm^2 area was scanned by 3D confocal microscopy, which was the counterpart of the sample actually used in electrolysis and as such was representative of a fresh surface. The high ratios for Anodes 1-5 show the roughness of these materials. Additionally, the variation between samples reflects the inherent inhomogeneity of each anode due to pores, and shows that Anode 1 in particular was very inhomogeneous.

The wetting of the anodes with alumina saturated-cryolite electrolyte at 1000 °C is illustrated in Figure 6. As shown by contact angles >90°, electrolyte did not wet graphite and anodes high in anisotropy well, while the more isotropic anodes had contact angles lower than 90° and were therefore better wetted. However, it should be noted that the anode materials were not polarised during the wetting experiments due to experimental limitations, meaning results do not directly reflect electrolysis conditions. Results may also be influenced by the specific location of the electrolyte on the anode, such as whether the droplet predominantly rested on a coke grain, the binder matrix composed of a mixture of binder and coke fines, or even a large pore. This variation could explain some of the asymmetry seen, such as for Anode 2. Differences in wetting have previously been explained by small variations in surface roughness, with some studies of other systems finding that increased roughness improves wetting [44-46]. Here, the wetting properties seem not to correlate well with the pore size distribution, or surface roughness, as seen when comparing Figure

3, 5 and 6. Therefore, it may be more likely that variation in wetting is due to variation in isotropy or possibly impurity concentrations, as also suggested by Qiu et al. [47]. The wetting angle of graphite with cryolite electrolyte in this study (~100°) was slightly lower than that recorded in other studies (120-130° [16]), possibly due to material or electrolyte composition differences.

3.2. Electrochemical measurements of bubble evolution

Figure 7a compares the measured voltage-time characteristics of graphite anodes with horizontal, vertical [40] or rod [39] geometry. When a vertical anode was used, only very small oscillations were observed, possibly due to the evolution of small bubbles from the surface. Some bubble noise is to be expected even on vertical anodes, as studies have shown that the surface of a stationary vertical anode can be covered by up to 20 % gas bubbles at any one time [27, 28]. A rod, with both horizontal and vertical surfaces, exhibited oscillations between the two former anodes. All following results were therefore obtained with the horizontal geometry shown in Figure 1a, to maximise the effects of bubbles during electrolysis.

Comparisons of the 8 mm diameter horizontal graphite anode used in this study with horizontal graphite anodes of 6, 10 and 14 mm diameter confirmed that the design was acceptable for use, and may give information about bubble size and coverage. As shown in Figure 7b, the surface of the 6 mm horizontal anode became completely blocked and was virtually unusable even at current densities as low as 0.1 A cm^{-2}. As this effect was not observed with the larger diameter anodes, this infers bubbles reached a maximum diameter of close to 6 mm. Additionally, potential oscillation magnitude and frequency were strikingly similar on the 8, 10 and 14 mm anodes for

the same current density, inferring a relatively similar limiting bubble volume and coverage despite changes in area.

During electrolysis at 1 A cm^{-2}, the graphite anode exhibited a clean "saw-tooth" curve potential oscillation (Figure 8). As bubbles formed, the potential increased due to a combination of increased ohmic resistance and hyperpolarisation due to a reduction in effective surface area from bubble coverage. Different stages of bubble growth could be identified; according to Einarsrud [13], the initial stage of bubble nucleation and growth is characterised by a linear growth in potential, credited to increased screening with increasing bubble number and size. When bubbles coalesce and grow, the potential fluctuates in a characteristic mid-section [13]. Subsequently when bubbles are released, resistance and effective surface area are immediately re-normalised, and the potential drops sharply. The smooth shape of the saw-tooth curve for the graphite anode in Figure 8, and the final linear increase of the potential, indicate that fine bubbles nucleated on the anode that eventually coalesced into a single bubble, which was eventually released. According to the image showing the distribution and size of the pores (Figure 4), the graphite anode only contained very small pores (i.e. possible nucleation sites) that were homogeneously distributed, which may have resulted in a large extent of coalescence occurring uniformly across the surface in a short amount of time. This could explain the steeper middle section of the saw-tooth curves.

In addition to graphite, bubble evolution was studied on Anodes 1 to 5 at near-industrial current densities. A comparison of potential *vs.* time measurements at 1 A cm^{-2} is shown in Figure 9, while summarised potential oscillation magnitudes for all

anodes are shown in Figure 10. For Anodes 1-5, the potential oscillation curves also exhibited a saw-tooth shape, with a steady increase in the measured potential, superimposed by minor oscillations of a high frequency, characteristic of bubble coalescence. The saw-tooth shape appears to be more pronounced for Anodes 1 and 2, whereas for Anodes 3-5 the minor oscillations occurred at a lower frequency. This indicates that either bubbles did not coalesce to the same extent or that the coalescence was distributed more evenly across the entire surface and time period, perhaps due to anode wettability variation or the fact that these anodes had large pores in addition to small. It is also apparent that the more isotropic anodes (Anodes 3-5) had lower potential oscillation, and therefore lower bubble-related voltage losses, associated with bubble formation and release. The trend of the potential base-lines for the series of anodes, relating to electrochemical reactivity, was very similar to that previously measured with other anode geometries [39, 40]; graphite had the highest potential (correspondingly lowest reactivity), Anodes 1-4 generally showed a small decrease in base-line potential and Anode 5 had the lowest potential. However, although changes in reactivity may be related to anode isotropy or metal impurity content [39, 40], as this paper focused on measuring the change in anode potential with bubble release (rather than absolute potential), potentials were not IR corrected and therefore cannot give information on reactivity.

Other studies monitoring bubbles on horizontal graphite anodes by their associated potential fluctuations recorded similar saw-tooth curves [12, 22]. Results in this study were similar to that found by Xue and Øye [12] - their 10 mm diameter graphite anode evolved one main bubble, leaving the anode surface completely free of bubbles afterwards. However, larger anodes are thought to sustain several bubbles

simultaneously [16]. The magnitude of voltage variation of graphite recorded in other studies at 1 A cm^{-2} has been lower; for example 0.1 V [22] or 0.3 V [21], but in both cases discrepancies are most likely related to the geometry of the anode. The first used a cup-shaped, slightly inclined anode, and the latter study used 24 mm diameter anodes with a 5° inclination and the lowest 1.5 mm unshielded. The shields in this study covered 2 mm each side of the anode, possibly also hindering bubble release. Although not focused on here, as others also observed [12, 21], the quality of the measured saw-tooth curve degraded after long periods of electrolysis; Kiss [48] suggests that whilst regular oscillations are observed for single bubbles, when many smaller bubbles are present, the combined effect of growing, coalescing and detaching results in more random appearing fluctuations. In this case surface conditioning and anode edge rounding are probably responsible.

The average number of bubbles released in a 200 second application of 1 A cm^{-2}, and Fast Fourier Transform analysis (FFT) of the potential *vs.* time measurements are shown in Figures 11 and 12. A major FFT peak at a frequency in the range 0.27-0.39 Hz was observed for the anodes, which corresponded well with the measured time of around 3 seconds for bubble release in each case. For Anodes 1-5, FFT major frequencies were 0.39 Hz, 0.33 Hz, 0.33 Hz, 0.27 Hz and 0.34 Hz respectively. Thus, the FFT major frequency correlated well with bubble time period for all anodes except for Anode 5, where the FFT major frequency was lower than the average bubble release time. Reasons for the latter discrepancy are not known, but may relate to more variation within the measurements, as seen in Figure 9. A good correlation between FFT major frequency and bubble release time was similarly obtained by Dorin and Frazer [21] for their horizontal 24 mm diameter graphite anode, although

others [19] found a discrepancy between bubble release times and major FFT frequencies, attributed to a lack of periodicity of bubble release possibly due to overlapping bubbles. Other peaks in the FFT spectrum have been related to small potential oscillations due to the growth and coalescence of bubbles.

The rise in potential during bubble formation is thought to be mainly due to partial screening of the anode surface [49]. Previous studies have, however, observed that potential oscillation magnitude is also related to gas layer thickness [49] and bubble size [24]. The average bubble volume at 1 A cm^{-2}, calculated from the average number of bubbles released in a 200 second application of 1 A cm^{-2}, is shown in Figure 13. Generally, bubble volume seemed to correlate with the content of large pores; i.e. of the petroleum coke anodes, Anodes 3 and 4 had both the largest bubble volumes and largest pores (*cf.* Figure 3a). Calculated gas volumes are close to 0.4-0.6 cm^3 cm^{-2} anode area, as predicted by Aaberg et al. [3] in their physical modelling study, if the real area of these anodes is considered. Figure 14 shows how bubble volume changed over time for one 200 second 1 A cm^{-2} application, calculated from the bubble time period before a major bubble release. After an initial conditioning period (first ~20 bubbles), CO_2 evolution from most anodes was stable over time, although bubbles from some anodes increased slightly in volume during the course of the experiment, in contrast to that observed in [12]. This may be due to the anode shielding, but is not fully understood.

As demonstrated by the potential oscillation magnitude, the more anisotropic anodes (Anodes 1 and 2) were less screened by bubbles than the graphite, but the bubbles formed were slightly larger and released at a lower frequency. As wetting properties

were similar, this may be related to differences in surface roughness and porosity. The estimated size of bubbles for the more isotropic Anodes 3 and 4, based on the frequency of bubble release, were the largest, although the magnitudes of potential oscillation and thus the screening of the surfaces were lower. Due to the fact that Anodes 3 and 4 had positive wetting interactions with electrolyte, it is possible that CO_2 produced at these anodes formed bubbles with a rounded shape, due to the higher contact angle. When CO_2 forms at the anode-electrolyte interface, bubbles are generally envisioned to take up the remaining contact angle (CA) from 180° (i.e. $180°\text{-}CA_{electrolyte}$), as described by Thonstad [50]. Thus, CO_2 residing on the anisotropic anodes will have a lower contact angle, and bubbles of similar volume will cause a larger screening of the surface. Variation in surface screening may also be due to variation in distribution of pores, considered as bubble nucleation sites, as shown in Figure 4.

Rough estimates of the degree of surface screening by bubbles were obtained from analysis of the current increase upon bubble release from CVs, assuming the current measured directly after a bubble evolution event corresponded to a completely unscreened anode surface. This confirmed the aforementioned variation; during the voltammetry scan, bubbles screened approximately 80% of the graphite surface before being evolved, but only 10% of the surface of Anode 4 (Figure 15), neglecting the surface roughness. By integration of charge passed, the volume of the bubbles released in Figure 15a from graphite was calculated as ~0.37 ml. This is close to the volume of graphite bubbles calculated in Figure 13.

In contrast to the other anodes, Anode 5 had a small calculated bubble volume, but both the magnitude of the potential oscillation, and the electrolyte wetting were similar to Anodes 3-4. As seen from Figure 4, there are differences in the pore size distribution, but information about the shape and depth of pores is presently lacking. It seems, however, that the release of small bubbles from Anode 5 may be related to the surface topography, but further work is needed in order to discuss these factors thoroughly. These differences compared to the other anodes may relate to the production of Anode 5 from pitch-based coke rather than petroleum coke.

Bubble release from the anodes was also studied at other current densities, as low as 0.1 A cm^{-2}. Lower current densities were not studied to avoid possible major electrochemical production of CO. Figure 16 shows the measured potential oscillation of graphite and Anodes 1 to 5 at selected current densities. The trend observed at 1 A cm^{-2} was generally also observed down to 0.2 A cm^{-2}. At the lowest current densities studied, 0.1 A cm^{-2}, the saw-tooth curve pattern completely broke down for Anodes 3 and 4 and few, if any, major bubbles were released. Due to the high permeability of these anodes (resulting from the high content of large pores) coupled to their small size, gas may escape through the anode. To estimate the extent of this phenomenon, Equation 2 was used. In 3.3 seconds, the average time period for a bubble release based on a frequency of 0.3 Hz, and assuming an overpressure based on the hydrostatic pressure experienced by CO_2 underneath the anode of 100 Pa, the gas volume that could escape through the anode pores was found to be ~1.8 x 10^{-6} ml. This was negligible when compared to a typical bubble volume of 0.5 ml. Even if the pores could act as a gas reservoir alone, their total volume was only ~0.4 ml, based on a total porosity of 12 %. Therefore either way, the throughput capacity provided by

the pores would not be enough to affect the dominant way that gas is released, i.e. released externally from the anode base.

As the current density was decreased below 1 A cm^{-2}, the bubble evolution frequency generally decreased more than what would be expected based on the charge passed (causing the increase in the corresponding calculated volume per major bubble). This is similar to what was observed by Aaberg et al. [3], who found that bubble release frequency increased significantly with current density beyond what would be expected - for example, a factor of 10 for a factor of 4 increase in current. Explanations for variation at lower current densities may be due to CO_2 having more time to re-dissolve in the electrolyte rather than be released as a gas bubble, changes in bath movement, or the fact that wetting properties depend on the electrolysis conditions, for example, the degree of polarisation.

The ohmic resistance relating to bubble build up, δR_s was measured by measuring impedance at a characteristic constant high frequency. Figure 17 shows that R_s oscillated in a saw-tooth curve, with a major oscillation frequency identical to that observed with potential. The minimum value of R_s in the saw-tooth curve relates to the case where the anode surface is unscreened by bubbles, R'_s. Although R_s measurements could not be performed simultaneously with potential measurements, Figure 17 shows R_s and the anode potential overlaid, with the measurement time (X axis) of each normalised for where the potential and R_s starts to increase. The small discrepancy may be related to the sampling time for R_s (approximately two seconds).

The contribution of the ohmic resistance resulting from the presence of bubbles, δR_s, to the total bubble-related voltage losses for the graphite anode in Figure 17 was estimated to be 0.08 V, thus contributing to 26 % of the total potential oscillation. Hyperpolarisation, resulting from changes in local current density, therefore accounted for the majority of the potential increase. The contributions of δR_s and η_h towards total potential change for the anodes are shown in Figure 18. The relative contributions of δR_s and η_h on the potential increase were similar on all anodes, as expected based on the linear current-voltage characteristics observed for these anodes [40].

4. Conclusions

In this work the electrolytic formation and release of bubbles were studied for graphite anodes, as well as for five different anodes made of industrial grade single source cokes originating from petroleum or pitch. The isotropy levels of the anodes were determined by optical texture analysis, and anodes were also characterised in terms of wetting properties (contact angle of saturated electrolyte under non-polarised conditions), porosity, surface pore size distribution, as well as surface roughness.

The electrolyte wetting properties appeared to be related to the impurity level or structure of the materials (the degree of isotropy, carbon crystallite size), and not to the surface roughness or pore size distribution. As the contact angle of bubbles formed on the anode surface is generally assumed to be affected by electrolyte wetting, it is also indirectly influenced by the isotropy of the material.

The potential oscillation curves indicated that the graphite electrode experienced a significant screening by bubbles, with coalescence and most likely growth of one large bubble. The anisotropic anodes were less screened by bubbles than the graphite, but the bubbles formed were slightly larger, and released at a lower frequency. As wetting properties were similar, this can be related to differences in surface roughness and porosity.

The more isotropic Anodes 3 and 4 were less screened by bubbles; bubbles were larger than those from the anisotropic anodes, but released at a lower frequency. This was attributed to the positive anode-electrolyte wetting interaction and corresponding lower contact angle of the CO_2 bubbles, as well as differences in the pore distribution. The isotropic Anode 5 deviated from 3 and 4, as the anode showed a low potential oscillation magnitude whilst bubbles were released at a high frequency. The exact reason for these differences is unknown, but expected to be related to the topography of the surface, including factors such as pore depth and surface geometry. These factors may be different from the other anodes due to the fact that Anode 5 was produced from a pitch-based coke, rather than a petroleum coke as with Anodes 1-4. Although the results obtained cannot be directly transferred to industrial operating conditions, they nonetheless provide some fundamental insights into factors governing bubble formation and release.

Acknowledgements

This work was financed by Norsk Hydro ASA and the Research Council of Norway, grant number 210899/030**.** Thanks are due for the great work performed by Aksel

Alstad at the NTNU workshop where fabrication of experimental parts was required, and to Ole Kjos and Egil Skybakmoen at SINTEF for their helpful contributions. Additional thanks are due to Tone Anzjøn at SINTEF who performed the wetting work, and to Kirsti Gulbrandsen and other laboratory employees within Norsk Hydro ASA who performed XRF analysis, density and permeability measurements.

References

1. T. E. Norgate, S. Jahanshahi and W. J. Rankin, *J. Cleaner Prod.*, **15**(8–9), p. 838-48 (2007).
2. H. Kvande and W. Haupin, *JOM*, **52**(2), p. 31-7 (2000).
3. R. J. Aaberg, V. Ranum, K. Williamson and B. J. Welch, in *Light Metals 1997*, R. Huglen, Editor, p. 341-6, The Minerals, Metals & Materials Society (TMS), Warrendale, PA (1997).
4. T. M. Hyde and B. J. Welch, in *Light Metals 1997*, R. Huglen, Editor, p. 333-40, The Minerals, Metals & Materials Society (TMS), Warrendale, PA (1997).
5. H. M. Zhu and J. Thonstad, in *Light Metals 2003*, P. N. Crepeau, Editor, p. 343-9, The Minerals, Metals & Materials Society (TMS), Warrendale, PA (2003).
6. O. S. Kjos, T. A. Aarhaug, H. Gudbrandsen, Å Solheim and E. Skybakmoen, in *10th AASTC*: Launceston, Tasmania, B. Welch, G. Stephens, J. Metson and M. Skyllas-Kazacos, Editors, 4b1, Copyright University of New South Wales: School of Chemical Engineering (2011).
7. O. S. Kjos, T. A. Aarhaug, E. Skybakmoen and Å Solheim, in *Light Metals 2012*, C. E. Suarez, Editor, p. 623-6, The Minerals, Metals & Materials Society (TMS), Warrendale, PA (2012).
8. G. Chen, Z. N. Shi, B. L. Gao, X. W. Hu and Z. W. Wang, *Trans. Nonferrous Met. Soc. China*, **22**(9), p. 2306-11 (2012).
9. F. Nordmo and J. Thonstad, *Electrochim. Acta*, **30**(6), p. 741-5 (1985).
10. K. E. Einarsrud and S. T. Johansen, *Prog. Comput. Fluid Dyn.*, **12**(2), p. 119-30 (2012).

11. K. E. Einarsrud, S. T. Johansen and I. Eick, in *Light Metals 2012*, C. E. Suarez, Editor, p. 875-80, The Minerals, Metals & Materials Society (TMS), Warrendale, PA (2012).

12. J. L. Xue and H. A. Øye, in *Light Metals 1995*, J. W. Evans, Editor, p. 265-71, The Minerals, Metals & Materials Society (TMS), Warrendale, PA (1995).

13. K. E. Einarsrud, PhD thesis, Norwegian Univeristy of Science and Technology (NTNU), Trondheim (2012).

14. B. L. Gao, X. W. Hu, J. L. Xu, Z. N. Shi, Z. W. Wang and Z. X. Qiu, in *Light Metals 2006*, T. J. Galloway, Editor, p. 467-70, The Minerals, Metals & Materials Society (TMS), Warrendale, PA (2006).

15. Y. F. Wang, L. F. Zhang and X. J. Zuo, in *Light Metals 2009*, G. Bearne, Editor, p. 581-6, The Minerals, Metals & Materials Society (TMS), Warrendale, PA (2009).

16. L. Cassayre, T. A. Utigard and S. Bouvet, *JOM*, **54**(5), p. 41-5 (2002).

17. D. Kasherman and M. Skyllas-Kazacos, *J. Appl. Electrochem.*, **21**(8), p. 716-20 (1991).

18. K. Qian, Z. D. Chen and J. J. J. Chen, *J. Appl. Electrochem.*, **28**(10), p. 1141-5 (1998).

19. K. E. Einarsrud and E. Sandnes, in *Light Metals 2011*, S. J. Lindsay, Editor, p. 555-60, The Minerals, Metals & Materials Society (TMS), Warrendale, PA (2011).

20. Z. W. Wang, B. L. Gao, H. T. Li, Z. N. Shi, X. D. Lu and Z. X. Qi, in *Light Metals 2006*, T. J. Galloway, Editor, p. 463-6, The Minerals, Metals & Materials Society (TMS), Warrendale, PA (2006).

21. R. Dorin and E. J. Frazer, *J. Appl. Electrochem.*, **23**(9), p. 933-42 (1993).

22. R. D. Peterson, N. E. Richards, A. T. Tabereaux, O. H. Koski, L. G. Morgan and D. M. Strachan, in *Light Metals 1990*, C. M. Bickert, Editor, p. 385-93, The Minerals, Metals & Materials Society (TMS), Warrendale, PA (1990).

23. L. Cassayre, G. Plascencia, T. Marin, S. Fan and T. Utigard, in *Light Metals 2006*, T. J. Galloway, Editor, p. 379-83, The Minerals, Metals & Materials Society (TMS), Warrendale, PA (2006).

24. M. A. Cooksey, M. P. Taylor and J. J. J. Chen, *JOM*, **60**(2), p. 51-7 (2008).

25. R. C. Dorward, *J. Appl. Electrochem.*, **13**(5), p. 569-75 (1983).

26. W. E. Haupin, *JOM*, **23**(10), p. 46 (1971).

27. J. A. Leistra and P. J. Sides, *J. Electrochem. Soc.*, **133**(3), p. C119-20 (1986).

28. J. A. Leistra and P. J. Sides, *Electrochim. Acta*, **33**(12), p. 1761-6 (1988).

29. J. A. Leistra and P. J. Sides, in *Light Metals 1986*, R. B. Miller and W. S. Peterson, Editors, p. 473-8, The Minerals, Metals & Materials Society (TMS), Warrendale, PA (1986).

30. M. W. Meier, R. C. Perruchoud and W. K. Fischer, in *Light Metals 2007*, M. Sorlie, Editor, p. 277-82, The Minerals, Metals & Materials Society (TMS), Warrendale, PA (2007).

31. D. S. Severo, V. Gusberti, E. C. V. Pinto and R. R. Moura, in *Light Metals 2007*, M. Sorlie, Editor, Warrendale, PA: The Minerals, Metals & Materials Society (TMS). 287-92 (2007).

32. H. Gudbrandsen, N. Richards, S. Rolseth and J. Thonstad, in *Light Metals 2003*, P. N. Crepeau, Editor, p. 323-8, The Minerals, Metals & Materials Society (TMS), Warrendale, PA (2003).

33. X. W. Wang, G. Tarcy, S. Whelan, S. Porto, C. Ritter, B. Ouellet, G. Homley, A. Morphett, G. Proulx, S. Lindsay and J. Bruggeman, in *Light Metals 2007*,

M. Sorlie, Editor, p. 299-304, The Minerals, Metals & Materials Society (TMS), Warrendale, PA (2007).

34. H. Vogt, *Electrochim. Acta*, **42**(17), p. 2695-705 (1997).

35. K. Y. Zhang, Y. Q. Feng, P. Schwarz, Z. W. Wang and M. Cooksey, *Ind. Eng. Chem. Res.*, **52**(33), p. 11378-90 (2013).

36. L. Edwards, N. Backhouse, H. Darmstadt and M. J. Dion, in *Light Metals 2012*, C. E. Suarez, Editor, p. 1207-12, The Minerals, Metals & Materials Society (TMS), Warrendale, PA (2012).

37. L. Edwards, F. Vogt, M. Robinette, R. Love, A, Ross, M. McClung, R. J. Roush and W. Morgan, in *Light Metals 2009*, G. Bearne, Editor, p. 985-90, The Minerals, Metals & Materials Society (TMS), Warrendale, PA (2009).

38. F. Vogt, R. Tonti, M. Hunt and L. Edwards, in *Light Metals 2004*, A. T. Tabereaux, Editor, p. 489-93. The Minerals, Metals & Materials Society (TMS), Warrendale, PA (2004).

39. R. J. Thorne, C. Sommerseth, E. Sandnes, O. S. Kjos, T. A. Aarhaug, L. P. Lossius, H. Linga and A. P. Ratvik, in *Light Metals 2013*, B. Sadler, Editor, p. 1207-11, The Minerals, Metals & Materials Society (TMS), Warrendale, PA (2013).

40. R. J. Thorne, C. Sommerseth, A. M. Svensson, E. Sandnes, L. P. Lossius, H. Linga and A. P. Ratvik, in *Light Metals 2014*, J. Grandfield, Editor, p. 1213-7, The Minerals, Metals & Materials Society (TMS), Warrendale, PA (2014).

41. S. Rorvik and H. A. Øye, in *Light Metals 1996*, W. Hale, Editor, p. 561-8, The Minerals, Metals & Materials Society (TMS), Warrendale, PA (1996).

42. S. Rorvik, M. Aanvik, M, Sorlie and H. A. Øye, in *Light Metals 2000*, R. D. Peterson, Editor, p. 549-54, The Minerals, Metals & Materials Society (TMS), Warrendale, PA (2000).

43. G. Routschka and H. Wuthnow, *Pocket manual refractory materials: design, properties, testing*, 3rd ed., p. 474. Vulkan-Verlag GmbH, Essen, Germany (2008).

44. S. Herminghaus, *Eur. Phys. J. E: Soft Matter Biol. Phys.*, **35**(6) 43 (2012).

45. T. S. Chow, *J. Phys.: Condens. Matter*, **10**(27), p. L445-51 (1998).

46. S. Ashokkumar, J. Adler-Nissen and P. Moller, *Appl. Surf. Sci.*, **263**, p. 86-94 (2012).

47. Z. Qiu, T. Sun, Y. Yue, K. Yao, K. Grjotheim, H. A. Øye and H. Kvande, in *Light Metals 1995*, J. D. Evans, Editor, p. 247-51, The Minerals, Metals & Materials Society (TMS), Warrendale, PA (1995).

48. L. Kiss and S. Poncsak, in *Light Metals 2002*, W. Schneider, Editor, p. 217-23, The Minerals, Metals & Materials Society (TMS), Warrendale, PA (2002).

49. J. Zoric and Å Solheim, *J. Appl. Electrochem.*, **30**(7), p. 787-94 (2000).

50. J. Thonstad, P. Fellner, G. M. Haarberg, J. Hives, H. Kvande and Å Sterten, *Aluminium Electrolysis*, 3rd ed., p. 109, Aluminium-Verlag Marketing & Kommunikation GmbH, Breuerdruck, Germany (2001).

Table 1

Anode	Degree of isotropy / AU		[Metals] / ppm	[S] / %	Density / g cm^{-3}	Permeability / nPm
	Fiber index	Mosaic index				
Graphite	0.09	0.19	66	0.00	1.771	0.2
Anode 1	0.21	0.15	683	0.94	1.603	0.8
Anode 2	0.16	0.18	932	2.40	1.627	0.4
Anode 3	0.07	0.26	1976	4.18	1.614	6.1
Anode 4	0.10	0.26	2430	4.45	1.596	6.9*
Anode 5	0.08	0.20	2413	0.37	1.648	4.0

Figure 1

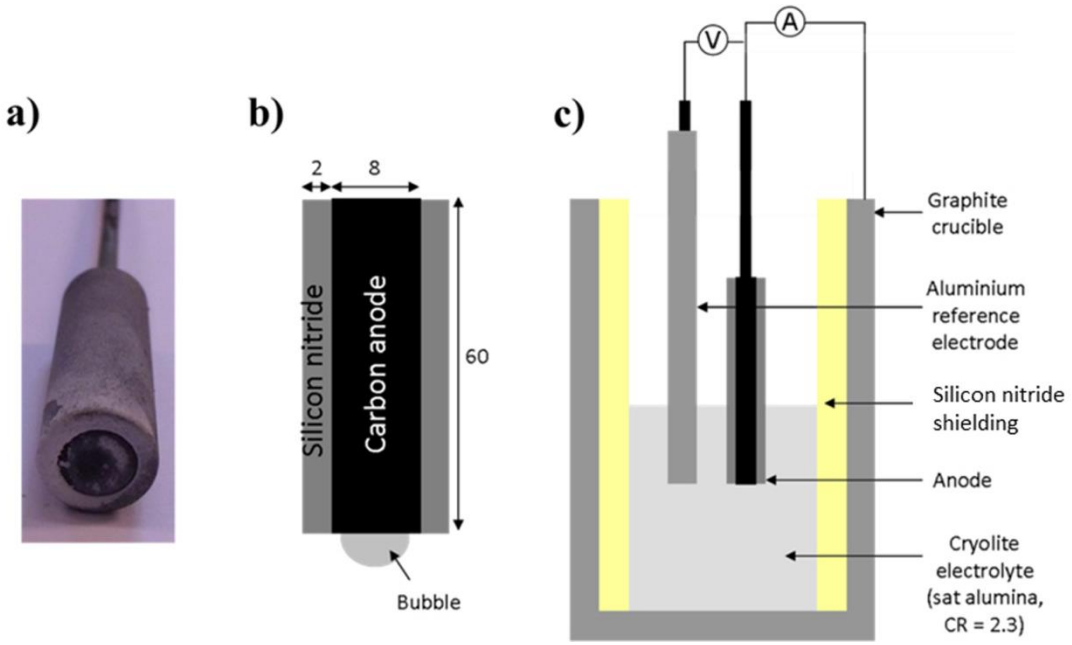
a)
b)
c)
2
8
60
Silicon nitride
Carbon anode
Bubble
V
A
Graphite crucible
Aluminium reference electrode
Silicon nitride shielding
Anode
Cryolite electrolyte (sat alumina, CR = 2.3)

Figure 2

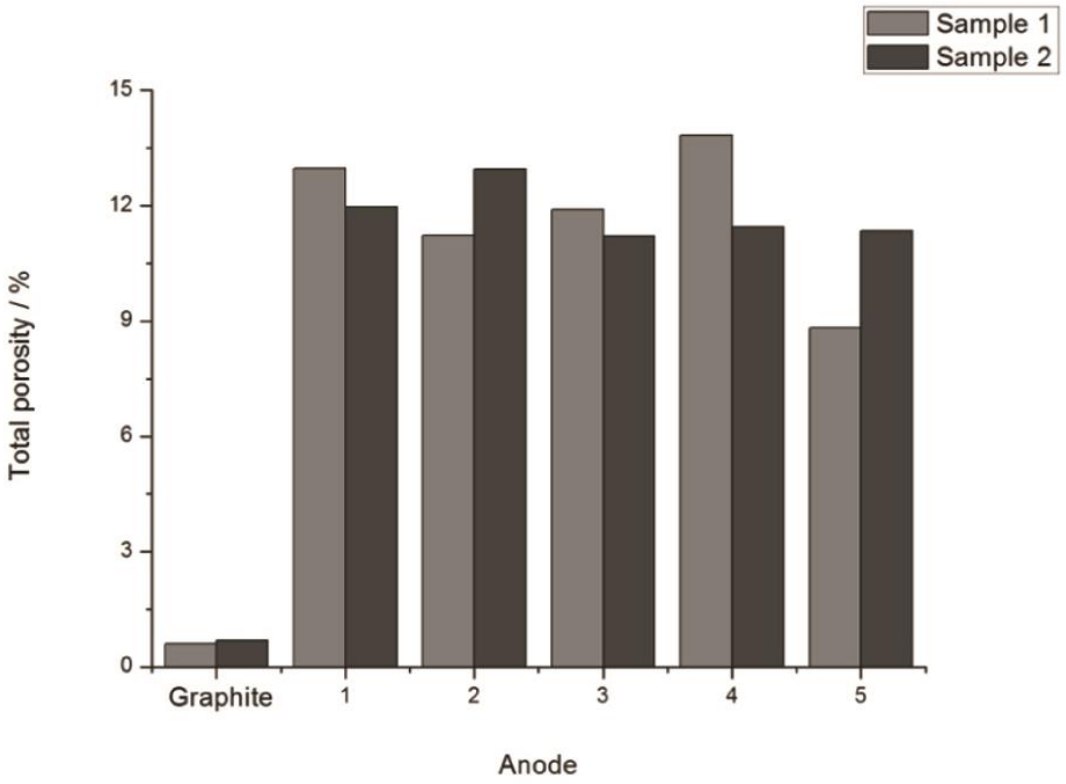
Sample 1
Sample 2
Total porosity / %
15
12
9
6
3
0
Graphite
1
2
3
4
5
Anode

Figure 3

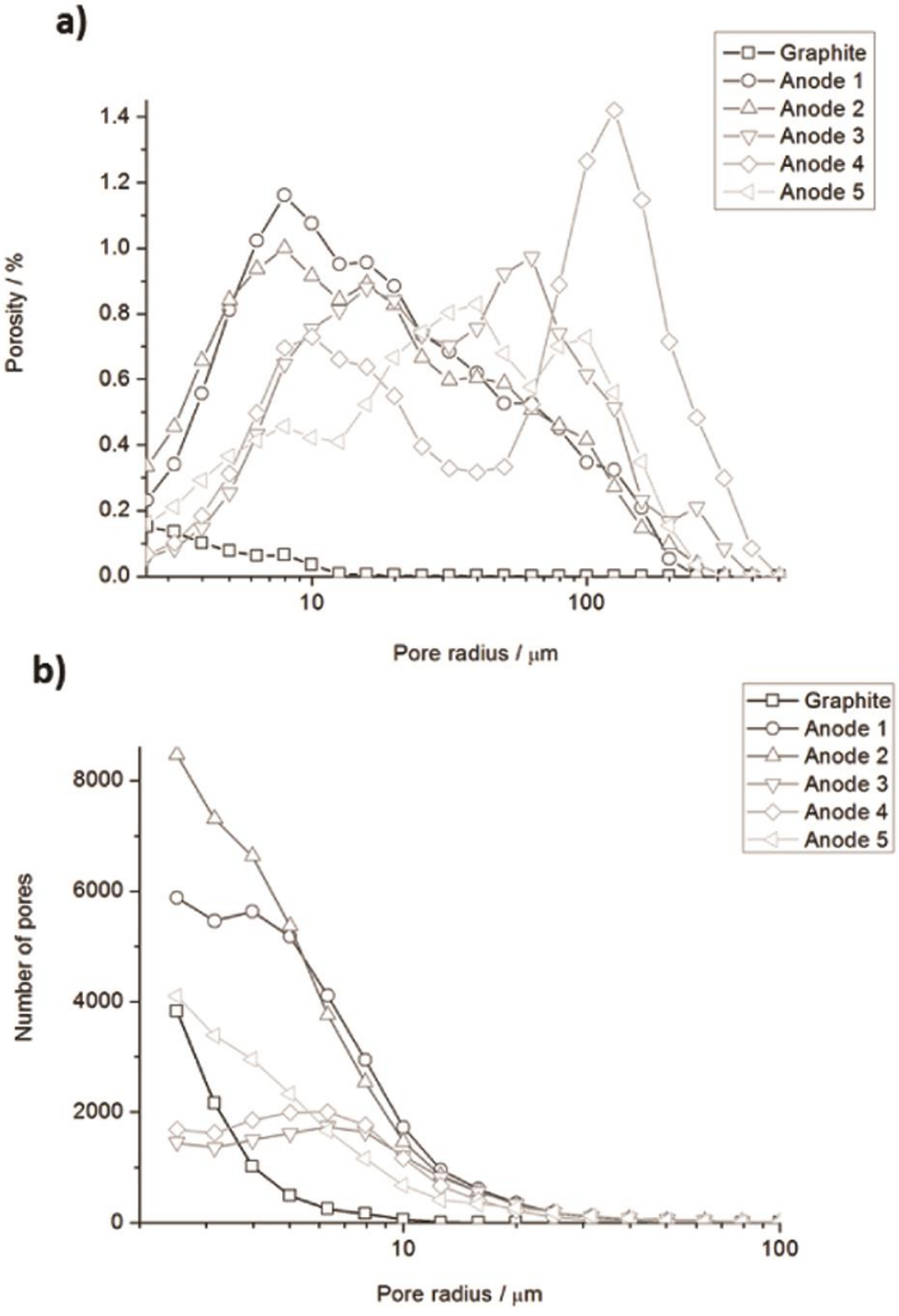
a)
Graphite
Anode 1
Anode 2
Anode 3
Anode 4
Anode 5
Porosity / %
1.4
1.2
1.0
0.8
0.6
0.4
0.2
0.0
10
100
Pore radius / μm
b)
Graphite
Anode 1
Anode 2
Anode 3
Anode 4
Anode 5
Number of pores
8000
6000
4000
2000
0
10
100
Pore radius / μm

Figure 4

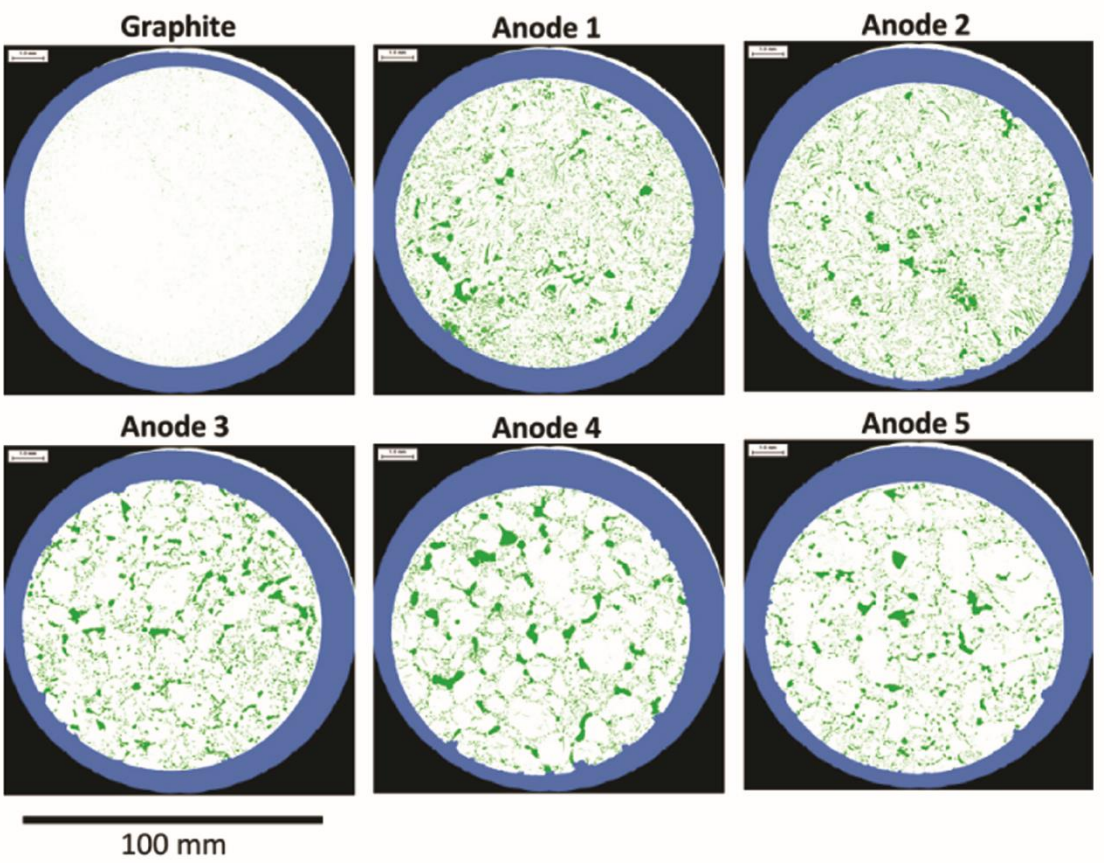

Figure 5

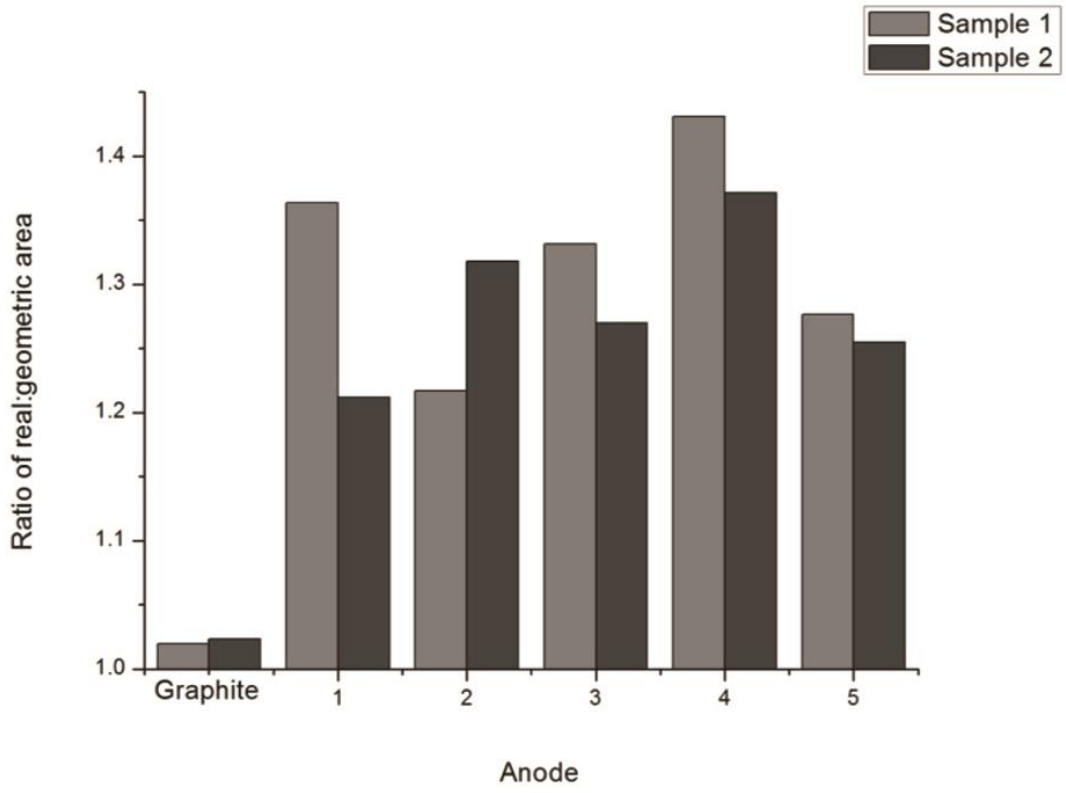
Sample 1
Sample 2
Ratio of real:geometric area
1.0
1.1
1.2
1.3
1.4
Graphite
1
2
3
4
5
Anode

Figure 6

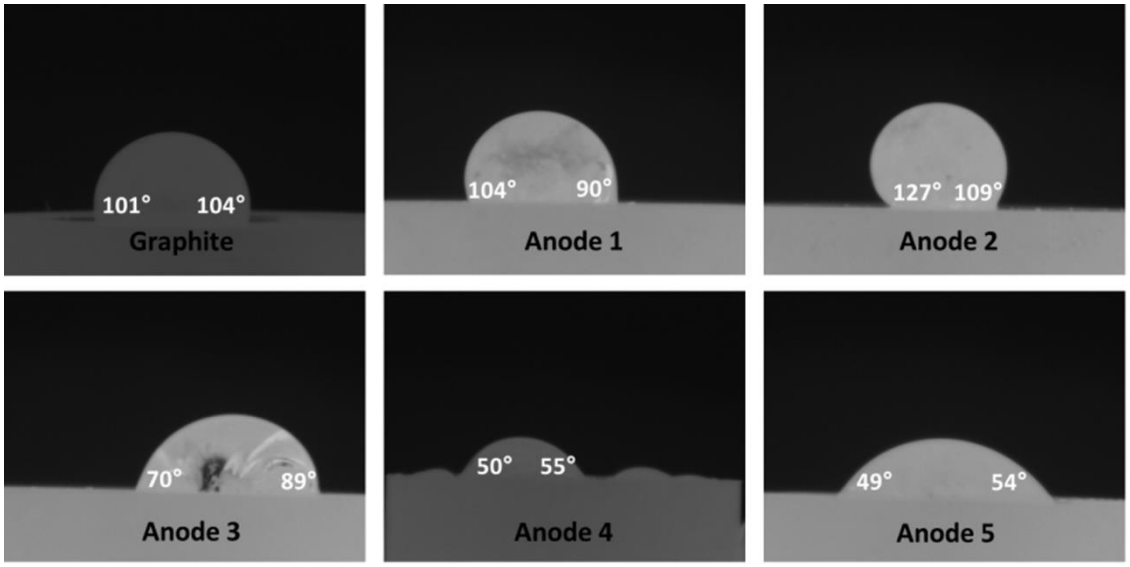
101° 104°
Graphite
104° 90°
Anode 1
127° 109°
Anode 2
70° 89°
Anode 3
50° 55°
Anode 4
49° 54°
Anode 5

Figure 7

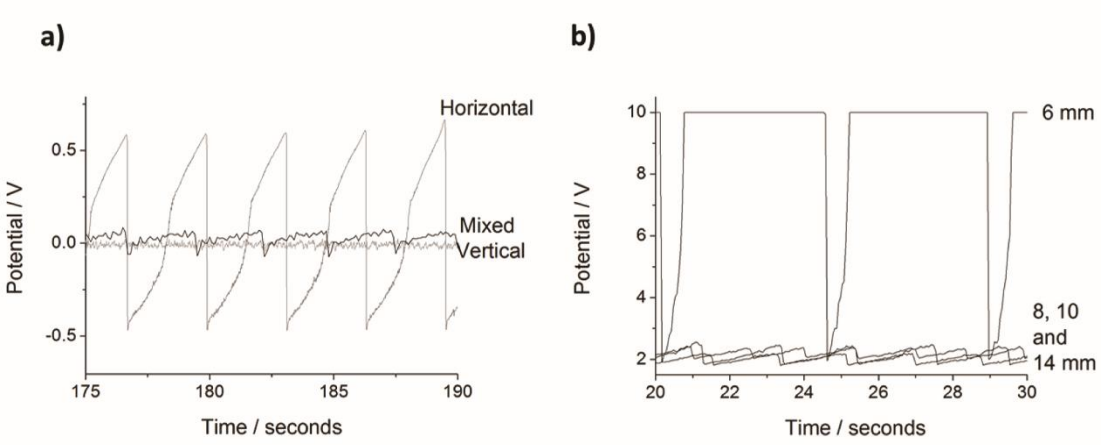
a)
Horizontal
Mixed
Vertical
Potential / V
0.5
0.0
-0.5
175
180
185
190
Time / seconds
b)
6 mm
8, 10
and
14 mm
Potential / V
10
8
6
4
2
20
22
24
26
28
30
Time / seconds

Figure 8

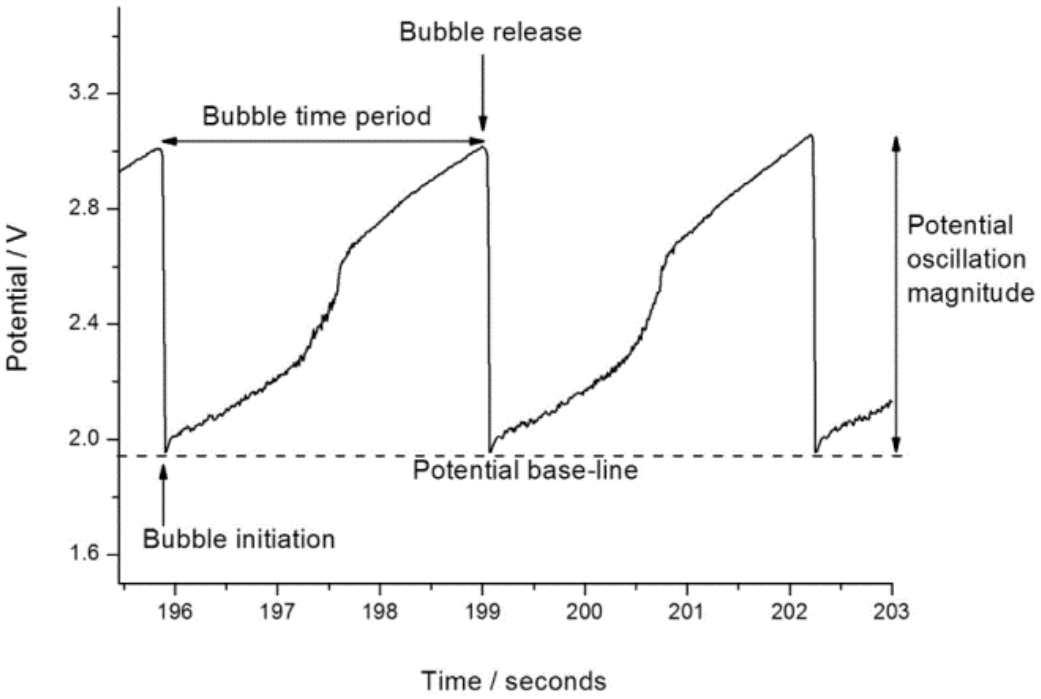
Bubble release
Bubble time period
Potential oscillation magnitude
Potential base-line
Bubble initiation
Potential / V
Time / seconds
3.2
2.8
2.4
2.0
1.6
196
197
198
199
200
201
202
203

Figure 9

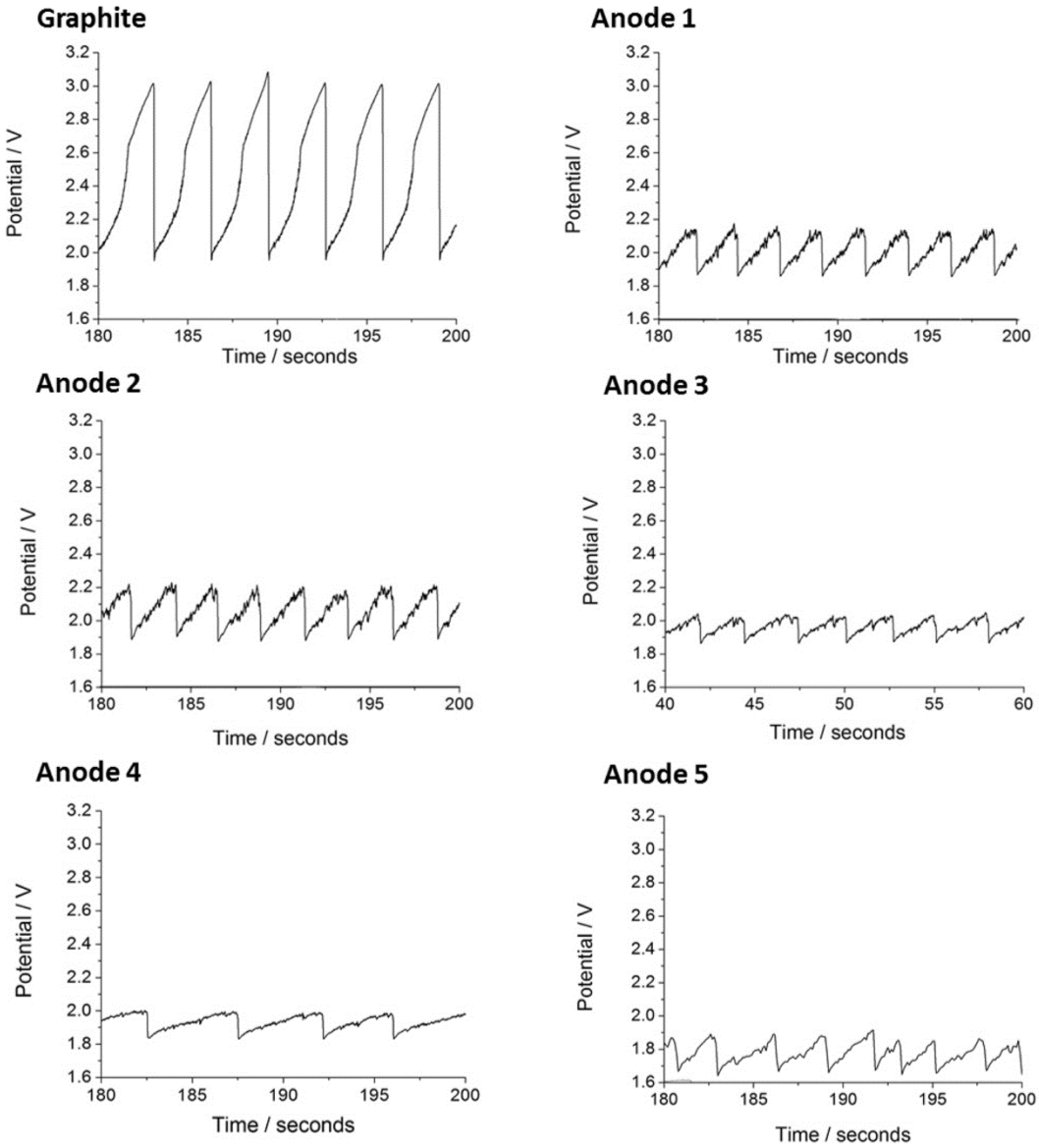
Graphite
Potential / V
Time / seconds
Anode 1
Potential / V
Time / seconds
Anode 2
Potential / V
Time / seconds
Anode 3
Potential / V
Time / seconds
Anode 4
Potential / V
Time / seconds
Anode 5
Potential / V
Time / seconds

Figure 10

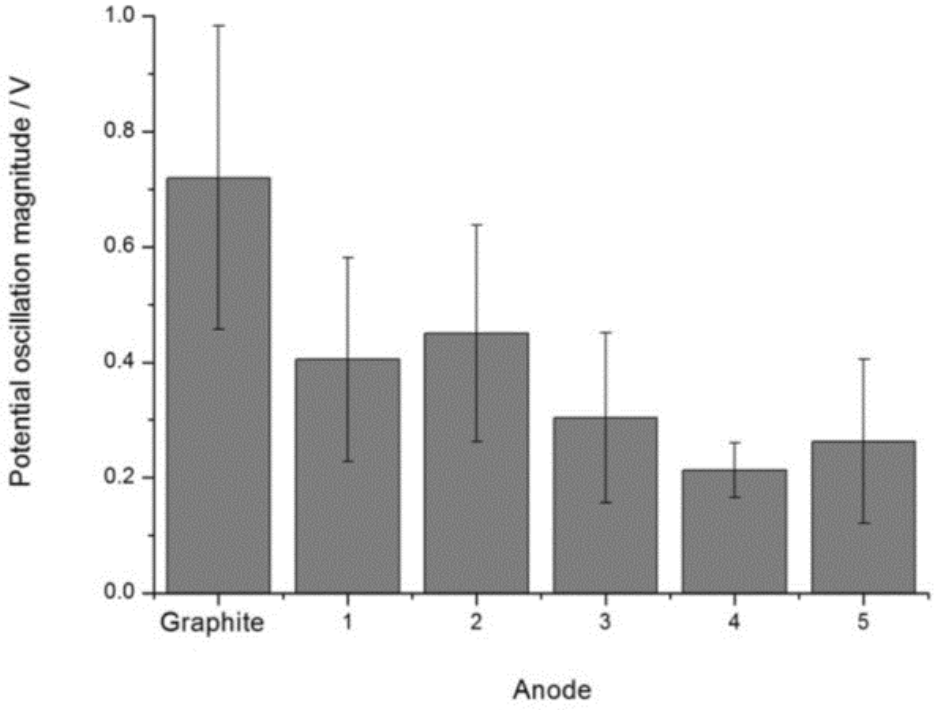
Potential oscillation magnitude / V
1.0
0.8
0.6
0.4
0.2
0.0
Graphite
1
2
3
4
5
Anode

Figure 11

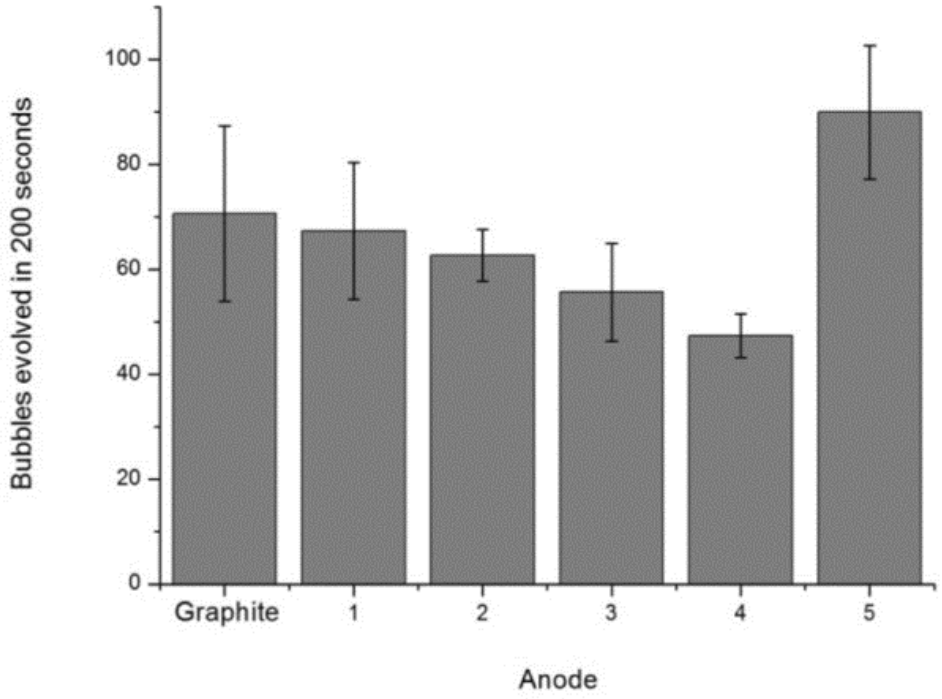
Bubbles evolved in 200 seconds
100
80
60
40
20
0
Graphite
1
2
3
4
5
Anode

Figure 12

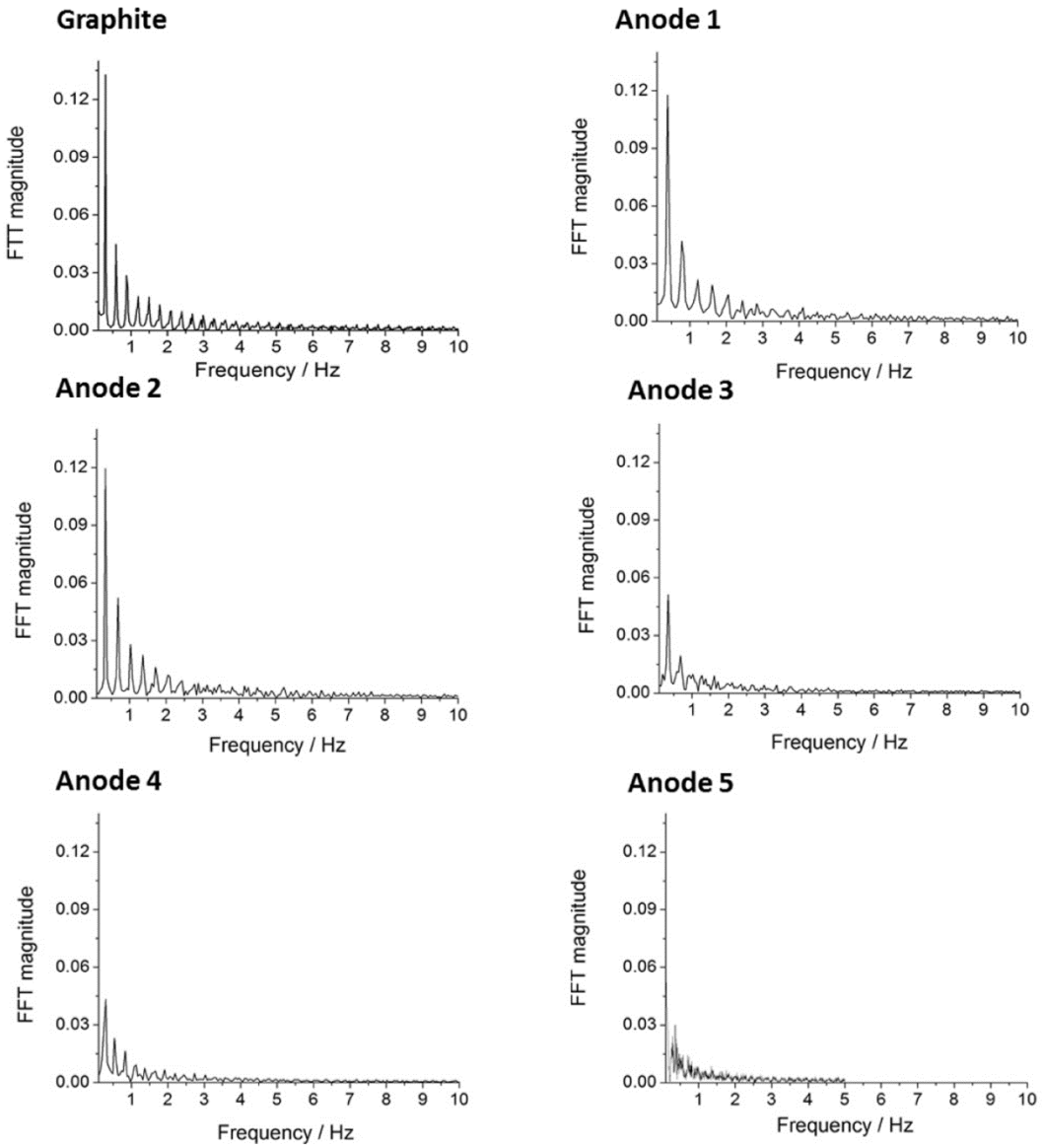
Graphite
FTT magnitude
Frequency / Hz
Anode 1
FFT magnitude
Frequency / Hz
Anode 2
FFT magnitude
Frequency / Hz
Anode 3
FFT magnitude
Frequency / Hz
Anode 4
FFT magnitude
Frequency / Hz
Anode 5
FFT magnitude
Frequency / Hz

Figure 13

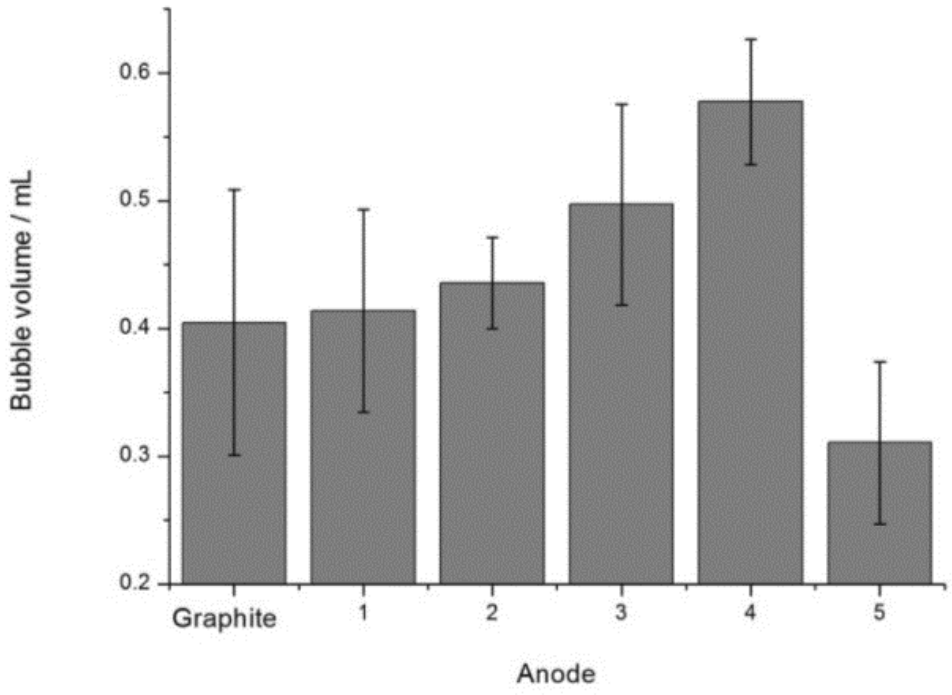

Figure 14

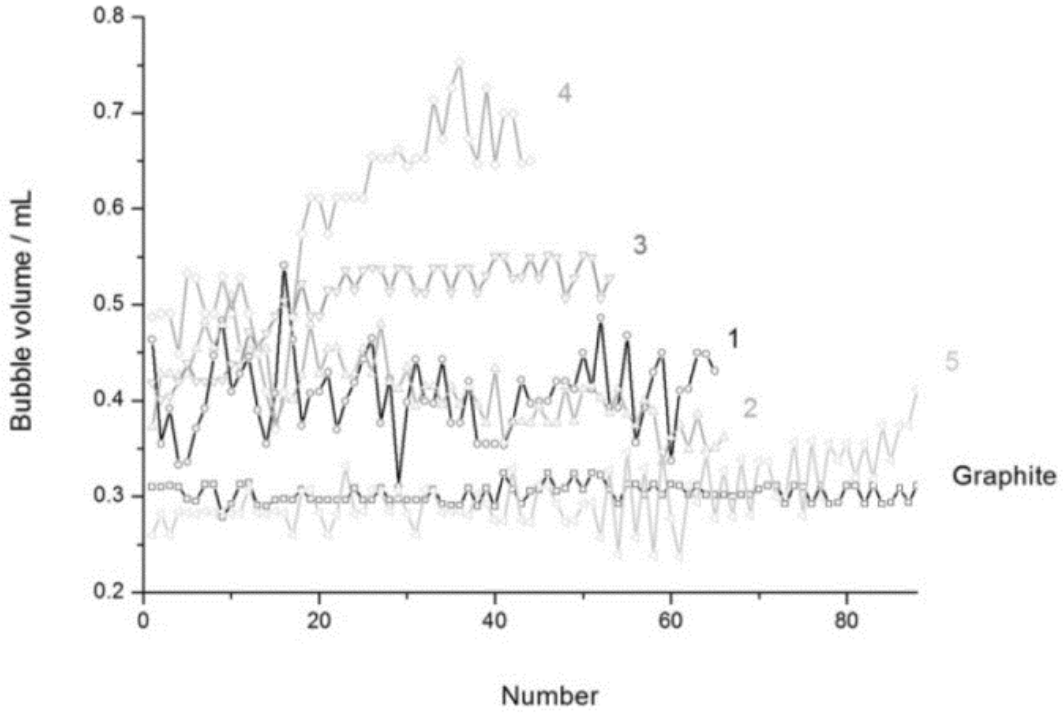
Bubble volume / mL
Number
0.2
0.3
0.4
0.5
0.6
0.7
0.8
0
20
40
60
80
1
2
3
4
5
Graphite

Figure 15

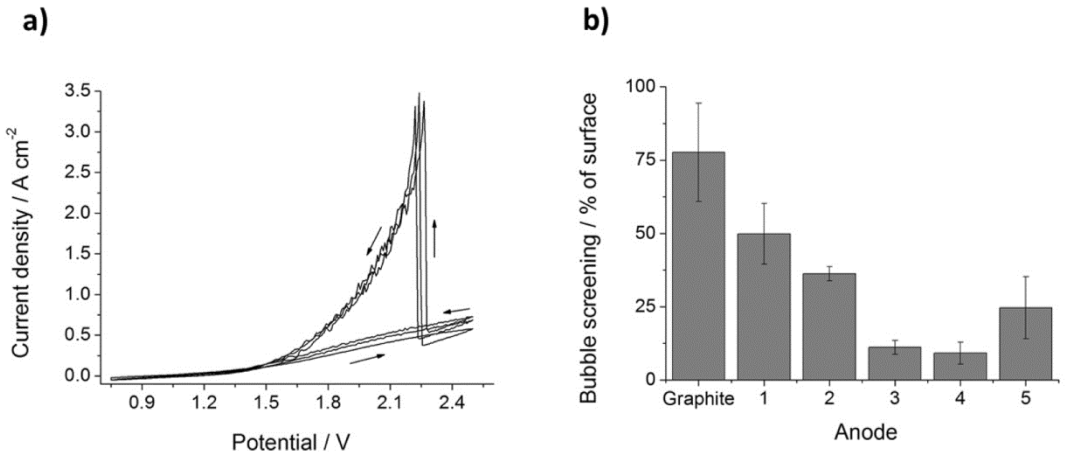
a)
Current density / A cm-2
3.5
3.0
2.5
2.0
1.5
1.0
0.5
0.0
0.9
1.2
1.5
1.8
2.1
2.4
Potential / V
b)
Bubble screening / % of surface
100
75
50
25
0
Graphite
1
2
3
4
5
Anode

Figure 16

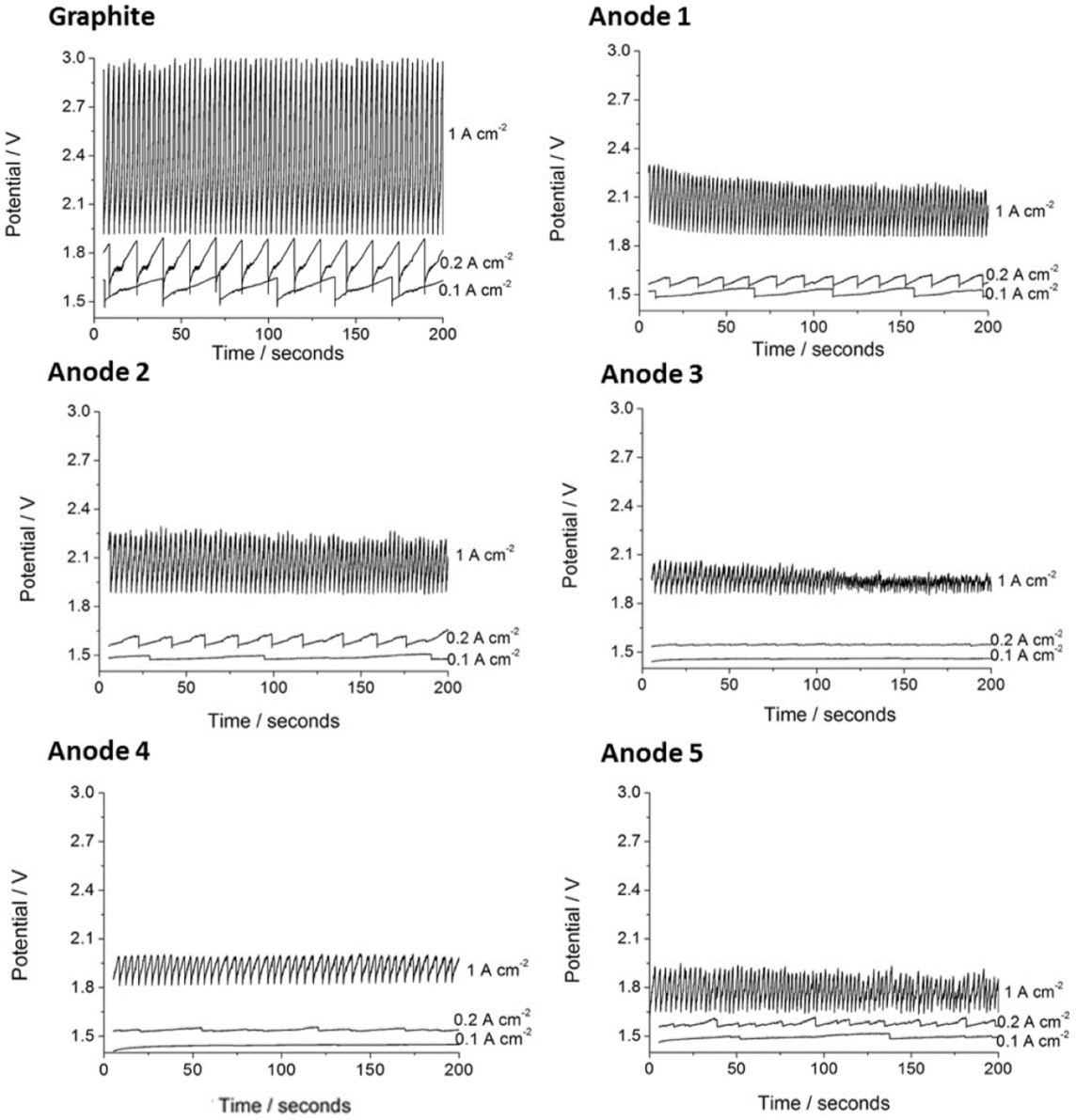
Graphite
Anode 1
Anode 2
Anode 3
Anode 4
Anode 5
Potential / V
Time / seconds
1 A cm-2
0.2 A cm-2
0.1 A cm-2

Figure 17

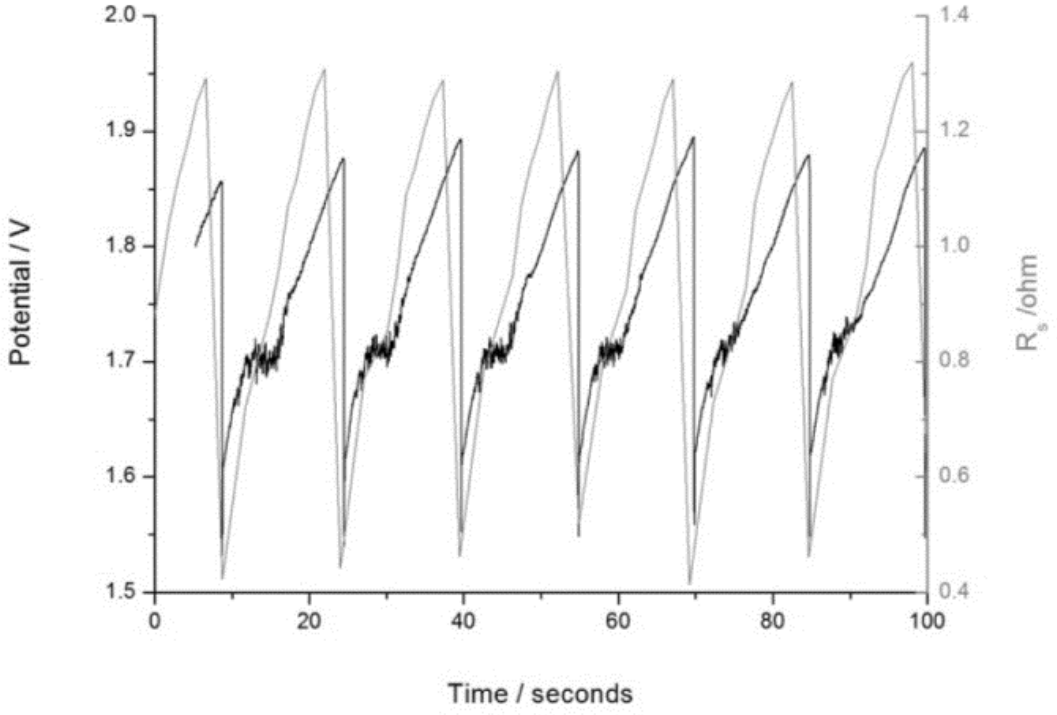
Potential / V
2.0
1.9
1.8
1.7
1.6
1.5
0
20
40
60
80
100
Time / seconds
1.4
1.2
1.0
0.8
0.6
0.4
R_s /ohm

Figure 18

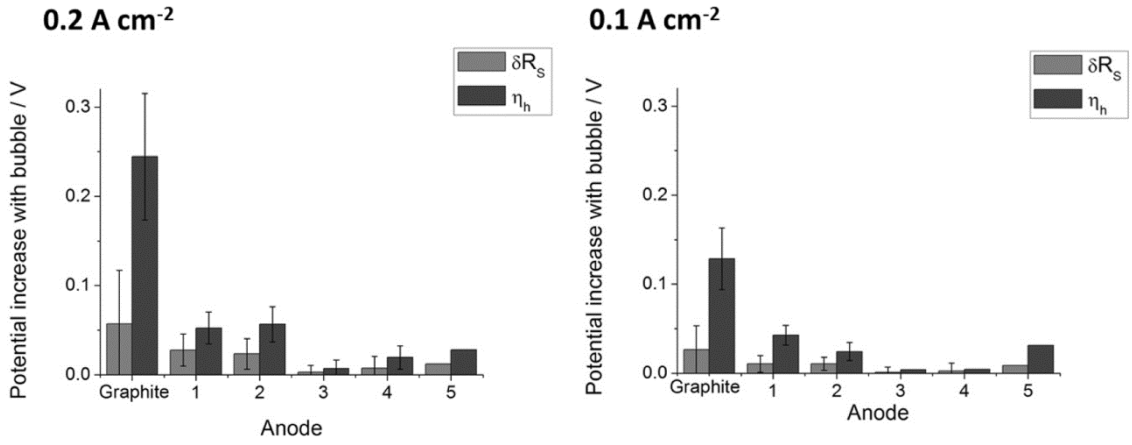
0.2 A cm-2
0.1 A cm-2
δRS
ηh
Potential increase with bubble / V
0.0
0.1
0.2
0.3
Graphite
1
2
3
4
5
Anode

Table and Figure Captions

Table 1. Selected anode properties. Summed metals include Na, Al, Si, Ca, V, Fe and Ni. Starred values indicate a result outside the range of testing. Anodes 1-4 were made with petroleum cokes and Anode 5 with a coal tar pitch based coke.

Figure 1. a. Photograph of the shielded horizontal anode. b. Schematic drawing of the anode geometry. c. Electrochemical cell with the carbon anode, graphite (cathode) crucible and aluminium reference electrode contained in a boron nitride casing as described in [7].

Figure 2. Total anode porosity. Data from two sample parallels is shown.

Figure 3. a. Anode pore size distribution. Data shown is an average of two sample parallels. b. Approximate number of pores in 0.50 cm^2, the area also used for electrochemical testing.

Figure 4. Porosity analysis images. Analysed pores within the limits of the anode boundaries (white circular area) are shown.

Figure 5. Anode real area (confocal) to geometric area ratios. Data from two sample parallels with 8 mm diameter is shown.

Figure 6. Wetting angles of electrolyte on anodes at 1000 °C. The diameter of each cryolite droplet was approximately 1 mm.

Figure 7. Anodic potential during electrolysis at 1 A cm^{-2} using a. graphite anodes with either horizontal, vertical or mixed (rod) geometry. Data is normalised around zero to show oscillation. and b. graphite horizontal anodes with different diameters.

Figure 8. Main characteristics of measured saw-tooth potential *vs*. time curve, using a graphite horizontal anode at 1 A cm^{-2}.

Figure 9. Measured anode potential *vs.* time during electrolysis at 1 A cm^{-2}.

Figure 10. Potential oscillation magnitude after 200 seconds electrolysis at 1 A cm^{-2}. Error bars show one standard deviation, where n = 6 for graphite and n = 3 for the industrial coke-based anodes.

Figure 11. Number of bubbles evolved during 200 seconds of electrolysis at 1 A cm^{-2}. Error bars show one standard deviation, where n = 6 for graphite and n = 3 for the industrial coke-based anodes.

Figure 12. FFT of potential oscillations. Only frequencies between 0.15-10 Hz are shown for clarity.

Figure 13. Average volume per major bubble evolved during 200 seconds of electrolysis at 1 A cm^{-2}. Error bars show one standard deviation, where n = 6 for graphite and n = 3 for the industrial coke-based anodes.

Figure 14. Volume of bubbles released consecutively during 200 seconds of electrolysis at 1 A cm^{-2}.

Figure 15. a. Example CVs at 0.1 V s^{-1} on a graphite anode, showing a marked increase in current around 2.2 V where a bubble was released during each scan. Three consecutive scans are shown. b. Percent of surface screened by bubbles, as calculated from major bubble evolution events on the CVs between 2.1 and 2.3 V. Error bars show one standard deviation, where n = 3-6.

Figure 16. Anode potential oscillation *vs.* time during electrolysis at 1 A cm^{-2}, 0.2 A cm^{-2} and 0.1 A cm^{-2}.

Figure 17. Anodic potential (black) and series (ohmic) resistance, R_s (grey) during electrolysis at 0.2 A cm^{-2}, measured consecutively on a graphite horizontal anode.

Figure 18. Potential increase with bubble build up due to δR_s or η_h on the different anode materials during electrolysis at 0.2 A cm^{-2} or 0.1 A cm^{-2}.